Journal of Zhejiang University-SCIENCE A (Applied Physics & Engineering) 2022 23(6):479-494
www.jzus.zju.edu.cn; www.springer.com/journal/11582
E-mail: jzus_a@zju.edu.cn

Research Article

https://doi.org/10.1631/jzus.A2100532

Design method for hypersonic bump inlet based on transverse pressure gradient

Shang-cheng XU, Yi WANG✉, Zhen-guo WANG, Xiao-qiang FAN, Bing XIONG

College of Aerospace Science and Engineering, National University of Defense Technology, Changsha 410073, China

Abstract: Transverse pressure gradient (TPG) is one of the key factors influencing the boundary layer airflow diversion in a bump inlet. This paper proposes a novel TPG-based hypersonic bump inlet design method. This method consists of two steps. First, a parametric optimization approach is employed to design a series of 2D inlets with various compression efficiencies. Then, according to the prescribed TPG, the optimized inlets are placed in different osculating planes to generate a 3D bump inlet. This method provides a means to directly control the aerodynamic parameters of the bump rather than the geometric parameters. By performing this method to a hypersonic chin inlet, a long and wide bump surface is formed in the compression wall, which leads to good integration of the bump/inlet. Results show that a part of the near-wall boundary layer flow is diverted by the bump, resulting in a slight decrease in the mass flow but a significant improvement in the total pressure recovery. In addition, the starting ability is significantly improved by adding the bump surface. Analysis reveals that the bump has a 3D rebuilding effect on the large-scale separation bubble of the unstarted inlet. Finally, a mass flow correction is performed on the designed bump inlet to increase the mass flow to full airflow capture. The results show that the mass flow rate of the corrected bump inlet reaches up to 0.9993, demonstrating that the correction method is effective.

Key words: Hypersonic bump inlet; Transverse pressure gradient (TPG); Boundary layer flow; Total pressure recovery; Starting ability; Mass flow correction

1 Introduction

Air-breathing hypersonic propulsion is a potential means for providing economical access to space and atmospheric flight (Huang et al., 2020). One form of air-breathing hypersonic propulsion is the supersonic combustion ramjet (scramjet), which has no rotating parts and must reach a certain speed and altitude for operation (Curran and Murthy, 2001). The promising high-speed performance of scramjet engines and their apparent potential for achieving near-orbital speeds have led to increasing attention towards hypersonic cruise missions, particularly the single-stage-to-orbit (SSTO) aerospace plane concept (Trefny, 1999; Curran, 2001). As one of the most crucial elements of scramjets, the inlet should provide sufficient high-quality airflow for combustion in a relatively wide operating range (Sziroczak and Smith, 2016; Xiong et al., 2019; Li et al., 2020; Zhang et al., 2020). However, when air flows through the forebody, a thick boundary layer develops due to viscous effect (Johnson and Lawing, 1977; Lawing and Johnson, 1978). If a large amount of low-energy boundary layer flow is swallowed by the inlet, the total pressure recovery coefficient will decrease and the starting performance will deteriorate (Zhang et al., 2014; Yue et al., 2018; Liu et al., 2019). Moreover, the captured airflow may be greatly separated by serious shock wave/boundary layer interactions, which can lead to the emergence of inlet unstart or even engine flameout (Bhanderi and Babinsky, 2005; Lau, 2008; Su et al., 2018). It was found that the boundary layer at the inlet entrance is strongly associated with the inlet layout, and its height can even reach half that of the inlet (Johnson and Lawing, 1977; Lawing and Johnson, 1978). For a well-designed inlet, the low-energy boundary layer should be excluded as much as possible to improve

✉ Yi WANG, wange_nudt@163.com
Shang-cheng XU, https://orcid.org/0000-0002-0717-8392
Yi WANG, https://orcid.org/0000-0002-3657-9769

Received Oct. 21, 2021; Revision accepted Jan. 4, 2022;
Crosschecked Apr. 14, 2022

the quality of the captured airflow (Ding et al., 2018; Im and Do, 2018).

To divert the boundary layer, a type of bump inlet was proposed in the last century (Simon et al., 1957). This bump inlet pre-compresses the incoming airflow using a 3D bump surface installed upstream of the inlet entrance while simultaneously excluding the boundary layer flow using the bump device. Compared with the boundary layer bleeding system, the bump inlet can effectively reduce the weight and aerodynamic drag of the vehicle (Schwartz et al., 2021; Yuan et al., 2021). Therefore, bump inlets have been widely adopted in supersonic aircraft (Yang, 2007). Numerous studies have focused on the influences of geometrical bump parameters to provide guidance for designing supersonic bumps (Kim and Song, 2008; Svensson, 2008; Kim, 2009; Lo and Kontis, 2017; Xu et al., 2017; Cheng et al., 2019). Xu et al. (2017) indicated that increasing the bump height could significantly improve the boundary layer diverting ability, and the flow loss could be greatly reduced by increasing the bump length. Svensson (2008) found that a long bump with a smooth beginning performed better than a blunt bump under supersonic conditions. Cheng et al. (2019) optimized a supersonic bump configuration using a parametric optimization method. By studying the working mechanism of the supersonic bump, it was found that the transverse pressure gradient (TPG) on the bump surface is the key element effecting boundary layer diversion (Kim and Sung, 2006; Colliss et al., 2014). Saheby et al. (2017) proposed a combination of the bump and waverider profile to increase the TPG. Saheby et al. (2016) and Yu et al. (2018, 2019) designed a bump configuration based on the ridge concept. The ridge acted as a slender vortex generator, creating a large pressure gap to divert the boundary layer significantly.

Previous studies on the design method and flow mechanism of the bump inlet under hypersonic conditions have been limited (Kim and Song, 2007; Tillotson et al., 2009). Results have indicated that directly introducing a supersonic bump into a hypersonic inlet would cause a large total pressure loss (Xu et al., 2019). The main contradiction was that the bump required a large TPG to remove the boundary layer, but strong shock waves would be induced by a high bump under hypersonic conditions. This revealed that the bump should be highly integrated with the hypersonic forebody. In view of this, Huang et al. (2018) and Yu et al. (2020) developed a design method for hypersonic bump/inlet integration based on a 3D inviscid inverse method. The inlet was installed on the bump surface, and the shocks induced by the inlet leading edge impinged on the cowl lip. Xu et al. (2019) proposed an integrated design method for a hypersonic forebody/bump. It was found that there was no additional flow loss in the highly integrated configuration. In addition, the results showed that the bump could improve the inlet starting ability, but the flow mechanism requires further investigation.

The TPG is one of the determining factors for the bump to divert the boundary layer. Therefore, the key in the bump configuration design is to properly arrange the TPG. However, there have been few studies on the bump design method based on the TPG. Moreover, the integrated design of the bump/inlet is a potential way to improve the inlet performance under hypersonic condition and should be further investigated.

This study focused on the design approach for a hypersonic bump inlet based on the TPG. In the proposed method, a parametric optimization is adopted to acquire 2D inlet configurations with different compression efficiencies. Then, the optimized inlets are placed in different osculating planes to generate a bump inlet. An integrated bump was formed in the compression wall by applying the design method to a hypersonic chin inlet. Then, the performances under the design conditions as well as the self-starting ability of the obtained bump inlet were evaluated. The results show that the bump inlet has distinct advantages in terms of total pressure recovery and starting performance. The flow mechanisms were analyzed based on numerical and experimental results. Finally, a mass flow correction was performed on the bump inlet to achieve full airflow capture.

2 TPG-based hypersonic bump inlet design

2.1 Study model

The proposed bump inlet design method was applied to a hypersonic chin inlet. As shown in Fig. 1, an axisymmetric forebody was adopted because of its ease of manufacture and high volumetric efficiency. According to the flow characteristics, the body

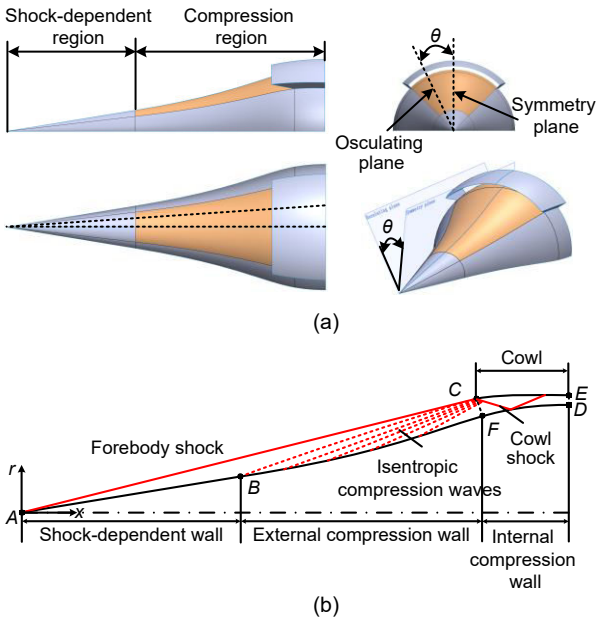

Fig. 1 Hypersonic chin inlet considered in this study: (a) multiple views of the inlet; (b) inlet configuration and flow structure in an osculating plane

was divided into shock-dependent and compression regions. The shock-dependent region was designed to generate a forebody shock wave. The external compression region adopts isentropic compression to reduce the flow loss (Xu, 2018). The cowl was installed at the chin of the vehicle. Two sweepforward sidewalls were employed to provide spillage windows for the large-scale separation bubble at the unstarting state. The design conditions were a flight Mach number of 6, flight height of 26 km, and attack angle of 0°. The forebody shock wave impinges on the cowl leading edge under the design conditions, achieving the shock-on-lip condition. According to the overall design requirements, the total contraction ratio (CR_t) was 6.0. Various internal contraction ratios (CR_{in}) could be obtained by adjusting the configuration of the compression wall. The streamwise plane passing the axis of symmetry is called the osculating plane. The angle from the plane of symmetry to the osculating plane is denoted by θ. The two sidewalls were located in the osculating planes of θ=−45° and 45°, respectively. Because the body is axisymmetric, the inlet profiles in the osculating planes (within the transverse range of $-45°\leqslant\theta\leqslant45°$) are identical.

To clarify the inlet operating process, the 2D inlet configuration and flow structure in an osculating plane are schematically illustrated in Fig. 1. The airflow is compressed by the forebody shock wave at first, and then isentropic compression waves are generated in the external compression wall *BF*. Subsequently, the compressed airflow is captured by the cowl *CE*. Finally, the airflow is further compressed in the internal contraction region to meet the demand for combustion.

2.2 TPG-based bump inlet design method

The proposed design method consists of two steps. First, various 2D axisymmetric inlet configurations with different compression efficiencies are designed using a parametric optimization method. Second, the optimized inlet configurations are arranged in different osculating planes of the 3D inlet based on the prescribed TPG. As such, an integrated bump inlet is obtained. The two steps are described in detail below.

2.2.1 Parametric optimization of 2D axisymmetric inlets

Considering the integrated design, inlet parameterization should be conducted under multiple geometric and aerodynamic constraints. To maintain the shock-on-lip condition, the shock-dependent wall *AB* and cowl *CE* are unchanged, and only the compression wall *BD* is parameterized. Moreover, the position and shape of the throat should remain constant, and the compression wall should remain horizontal at the throat to ensure smoothness between the inlet and downstream isolator.

Fig. 2 illustrates the parameterization method used to design the compression wall. It can be seen that the curve *BD* is parameterized utilizing the 3rd quasi-uniform B-spline (QUBS) and is controlled by four points. The first point *B* and end point *D* are fixed, but the middle points P_1 and P_2 are flexible. P_1 can move along the extension line of the shock-dependent wall *AB* to ensure wall smoothness at *B*. P_2 has the same height as *D* in the radial direction and can move along the horizontal direction to ensure that the

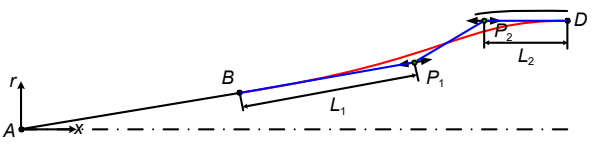

Fig. 2 Parameterization method for designing the compression wall

parameterized curve is horizontal at the throat. The distances from B to P_1 and from P_2 to D are denoted by L_1 and L_2, respectively. Inlet configurations with various compression walls can be acquired by adjusting the values of L_1 and L_2. In the current optimization method, L_1 and L_2 are employed as the design variables.

To improve the captured airflow quality as much as possible, the mass-averaged total pressure recovery coefficient at the throat (σ) was employed as one of the optimization objectives. In addition, the compression efficiency is largely determined by the internal contraction ratio under a constant total contraction ratio. An inlet with a small internal contraction ratio tends to exhibit high compression efficiency. Therefore, the internal contraction ratio was adopted as another goal. Moreover, the mass flow rate (φ) is a key parameter in the inlet design, which directly affects the engine thrust. For the researched inlet, when the mass flow rate satisfied $|\varphi-1|\leqslant 0.01$, the inlet was considered to have achieved full airflow capture. Therefore, the mass flow rate was employed as a constraint in the optimization. When a parameterized inlet realizes full flow capture, it can be regarded as a feasible inlet. In conclusion, the inlet optimization problem can be described as follows:

$$\begin{aligned}&\text{Objective: } \max(\sigma,\ -\mathrm{CR}_{\mathrm{in}})^{\mathrm{T}},\\&\text{subject to } |\varphi-1|\leqslant 0.01.\end{aligned}\tag{1}$$

An optimization platform was employed to solve the optimization problem. First, a 2D inlet configuration was designed for a group of variables. Then, the grid was auto-generated, and the inlet flow field was calculated numerically. Subsequently, a data processing module was used to obtain the geometric and aerodynamic parameters (σ, $\mathrm{CR}_{\mathrm{in}}$, φ). Subsequently, the parameters were evaluated by the optimization algorithm, and the variables were re-assigned to start the next optimization loop.

The multi-objective optimization algorithm of non-dominated sorting genetic algorithm-II (NSGA-II) was chosen for this study to solve the optimization problem. The population size and number of generations were 24 and 30, respectively. The crossover probability was set to 0.9. Fig. 3 shows the distribution of the optimized feasible inlets in $\mathrm{CR}_{\mathrm{in}}$–$\sigma$ pairs. Each point in the figure represents the performance

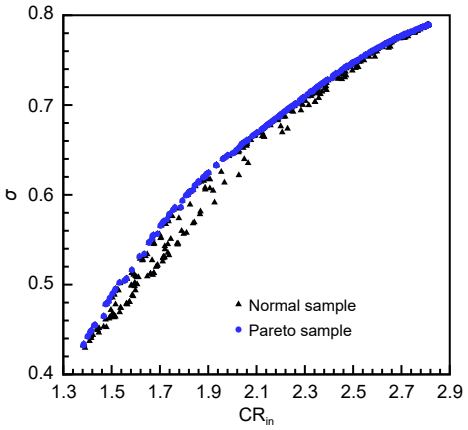

Fig. 3 Distribution of the optimized feasible inlets in $\mathrm{CR}_{\mathrm{in}}$–$\sigma$ pairs

parameters of a feasible inlet. It can be seen that the total pressure recovery coefficient gradually increases as the internal contraction ratio increases. In addition, a Pareto front (denoted by the circular points in Fig. 3) was formed. The inlet located in the Pareto front has the highest total pressure recovery coefficient among the inlets with a constant internal contract ratio.

Fig. 4a displays the configurations and the wall pressure distributions of typical inlets locating in the Pareto front. The compression walls of these inlets show significant difference. The smaller the internal contraction ratio is, the higher the compression wall is. The pressure curves of all the inlets exhibit two obvious rises in the compression region. The first slow pressure rise is caused by the external compression upstream of the inlet entrance, and the second rapid pressure rise is caused by the cowl-lip shock wave impingement. Herein, the first pressure rise is focused on. As shown in Fig. 4b, the wall pressures at x=1.2 m are plotted as a function of the internal contraction ratio. A steady pressure drop can be seen as the internal contraction ratio increases. For example, the pressure p of the inlet with $\mathrm{CR}_{\mathrm{in}}$=1.6 reaches up to $8.46p_\infty$ (p_∞ is the static pressure of the freestream), while that of the inlet with $\mathrm{CR}_{\mathrm{in}}$=2.6 is less than $4.30p_\infty$, exhibiting a significant pressure difference.

2.2.2 Bump inlet design based on the prescribed TPG

As the second step, the optimized 2D inlets are placed in the corresponding osculating planes based on the prescribed TPG to generate the bump inlet. Compared with conventional bump inlet design methods, this method provides a potential way to directly

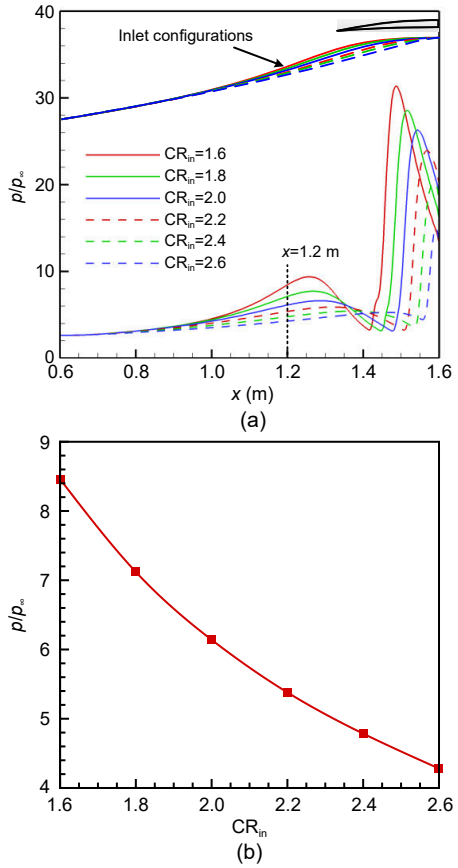

Fig. 4 Wall pressure distributions of typical Pareto-optimal inlets with different internal contraction ratios: (a) wall pressure curves along the flow direction; (b) wall pressures at x=1.2 m

control the aerodynamic parameters of the bump. In addition, the proposed method can significantly improve the inlet performance parameters owing to the utilization of the optimized inlets.

In this study, the TPG distribution in the plane of x=1.2 m was used to perform the design process. As expressed by Eqs. (2) and (3), the TPG distribution is a quadratic polynomial. Fig. 5a shows the TPG curve along the transverse direction. The curve can be uniquely defined by three parameters: θ_1, θ_2, and κ. θ_1 and θ_2 represent the start and end positions of the TPG, respectively, which jointly determine the range of the bump surface in the transverse direction. κ is the maximum value of the TPG, which is associated with the bump height. The transverse pressure (TP) distribution can be obtained by integrating Eq. (2). The solved TP is expressed by Eq. (4) and plotted in Fig. 5b. Herein, p_r is a constant term, which is associated with the compression efficiency of the designed

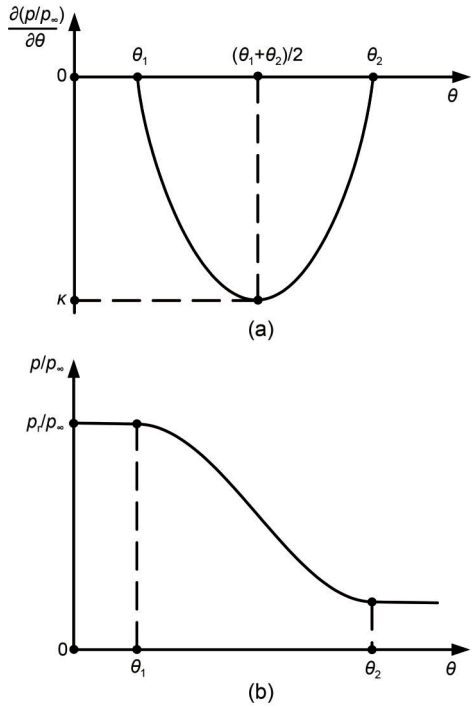

Fig. 5 Prescribed TPG (a) and TP (b) distributions in the plane of x=1.2 m

bump inlet. By changing the value of p_r/p_∞, the internal contraction ratio of the bump inlet can be controlled.

$$\frac{\partial\left(\frac{p}{p_\infty}\right)}{\partial(\theta)} = a\theta^2 + b\theta + c, \tag{2}$$

$$\begin{cases} a = -\dfrac{4\kappa}{\left(\theta_1-\theta_2\right)^2}, \\ b = \dfrac{4\kappa\left(\theta_1+\theta_2\right)}{\left(\theta_1-\theta_2\right)^2}, \\ c = -\dfrac{4\kappa\theta_1\theta_2}{\left(\theta_1-\theta_2\right)^2}, \end{cases} \tag{3}$$

$$\frac{p}{p_\infty} = \frac{a\theta^3}{3} + \frac{b\theta^2}{2} + c\theta + \frac{p_r}{p_\infty}. \tag{4}$$

The TPG and TP distributions in the plane of x=1.2 m can be obtained by assigning a group of θ_1, θ_2, κ, and p_r/p_∞. Then, to meet the preset pressure distribution, the Pareto-optimal inlets are placed in different osculating planes according to the relationship between the wall pressure and internal contraction ratio, as shown in Fig. 4b. Consequently, an integrated bump inlet configuration can be obtained. The parameters

chosen for this study were as follows: θ_1=0°, θ_2=60°, κ=0.075, and p_t/p_∞=7.7563. Under these parameters, the acquired bump surface was limited in the transverse range of −60°≤θ≤60°, the pressure difference on the bump surface was $3p_\infty$ (in the plane of x=1.2 m), and the internal contraction ratio of the bump inlet was 1.9.

For comparison, an inlet without a bump surface was designed as the original inlet. The Pareto-optimal inlet with CR_{in}=1.9 was placed in every osculating plane of the original inlet. Thus, the body of the original inlet was axisymmetric, and its internal contraction ratio was also 1.9. It is worth noting that the original inlet already has a high total pressure recovery performance due to the adoption of the optimized inlet configuration.

Figs. 6a and 6b show the geometrical configurations of the original inlet (dull red) and bump inlet (grey). Fig. 6c compares the profiles of both inlets in different cross-sections. The two inlets have the same shock-dependent wall and cowl, while an obvious difference can be seen in the compression wall. Compared with the original inlet, the compression wall of the bump inlet was higher in the central region but lower at both sides. This means that the entire compression wall can be regarded as a bump configuration, achieving a high integration of the bump/inlet.

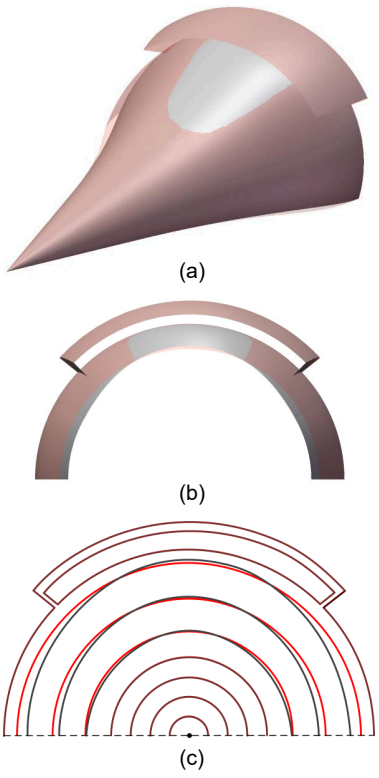

Fig. 6 Comparison of original inlet (dull red) and bump inlet (grey): (a) 3D view; (b) front view behind the plane of x=1.2 m; (c) profiles in different cross-sections (original inlet in red curves and bump inlet in black curves)

2.2.3 Validation of proposed design method

To validate the feasibility of the proposed method, a numerical simulation was utilized to calculate the inlet flow fields under the design conditions. Fig. 7 shows the TP and TPG distributions of the prescribed and actual results. As can be seen, the actual TP was essentially the same as the preset value except for an insignificant gap at the lateral border of the bump surface. Moreover, there is good consistency between the two TPG curves in the range of θ=0°–25°. Owing to the transverse flow on the bump surface, the actual TPG was slightly different from the prescribed value outside θ=25°. Overall, it is considered that the acquired bump inlet essentially meets the prescribed TP and TPG, demonstrating that the design method is feasible.

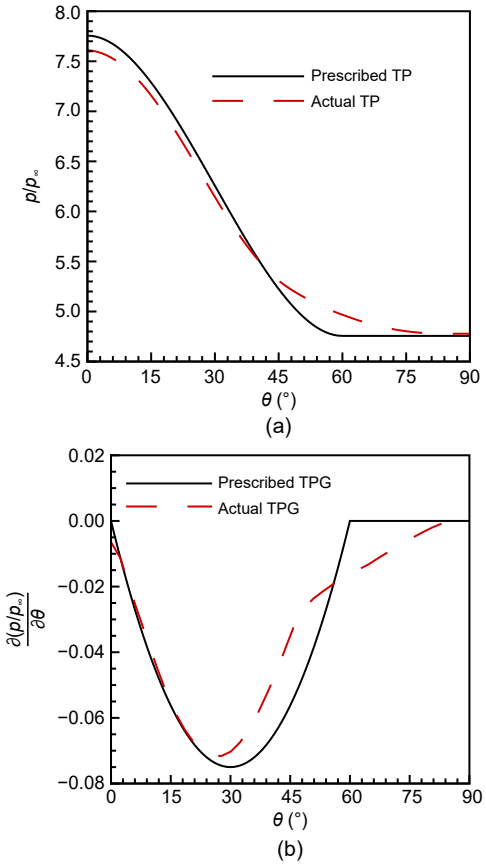

Fig. 7 TP (a) and TPG (b) distributions of the prescribed and actual results

Fig. 8 shows the wall pressure contours on the walls of the original and bump inlets. The pressure of the original inlet was uniformly distributed along the transverse direction. In contrast, the pressure of the bump inlet was high in the central area but low at the two sides, forming the TPG throughout the compression region.

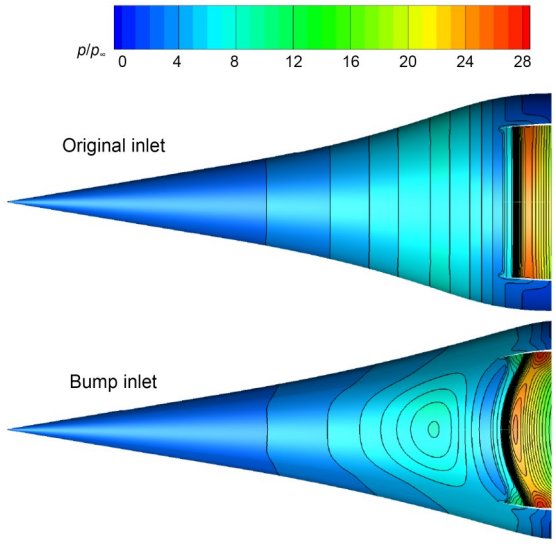

Fig. 8 Wall pressure contours of the original and bump inlets under design conditions

3 Experimental setup and numerical method

3.1 Experimental setup

The experiments in this study were conducted in a free-jet hypersonic wind tunnel at the National University of Defense Technology Scramjet Laboratory, China. Fig. 9 shows a schematic diagram of the wind tunnel, which consists of a high-pressure air supply system, electric heater, settling chamber, axisymmetric Laval nozzle, test chamber, vacuum tank, and some valves. The test model can be installed on a support device at different pitch angles to adjust the inlet attack angle. The wind tunnel can operate at an incoming Mach number of 5 with a usable test time of more than 60 s. Necessary measuring devices, such as a schlieren visualization system and pressure measurement system, are equipped to record the flow characteristics.

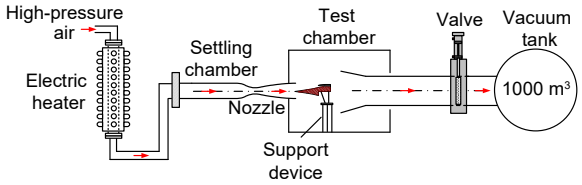

Fig. 9 Schematic diagram of the experimental free-jet wind tunnel

3.2 Numerical method

Two-dimensional Reynolds-averaged Navier–Stokes (RANS) equations were employed to simulate the 2D inlet flow fields during the optimization process. In addition, 3D RANS equations were adopted to solve the flow fields of the original and bump inlets. The air was assumed to be an ideal gas with viscosity modeled according to the Sutherland law. Considering the separated flows and complex shock system in the flow fields, the turbulence model of shear stress transport (SST) k-ω was chosen to solve the RANS equations.

Fig. 10 displays the computational domains and grids of the 2D and 3D inlets. To reduce the computational cost, the flow field in the symmetry plane was simulated for the 2D axisymmetric inlet, and only half of the model was calculated for the 3D inlet. A structured grid was generated in all computational domains. The grid points near the inlet entrance and the internal contraction region were clustered to accurately simulate the complex flow phenomena, such

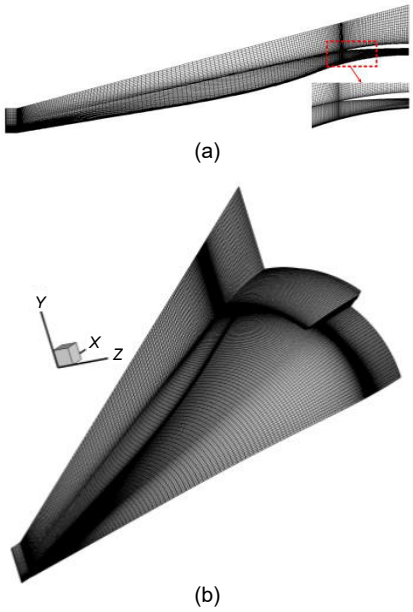

Fig. 10 Computational domains and grids of the inlet models: (a) 2D axisymmetric inlet; (b) 3D inlet (grid in the wall and symmetry plane)

as large-scale separation bubble and shock wave/boundary layer interactions. In addition, the boundary layer grid was set to calculate the near-wall flow as accurately as possible, and a value of $y+$ less than 1 was achieved in the main portion of the wall flow region. The boundary conditions of the inflow and outflow were set as the pressure far-field and pressure outlet, respectively. No-slip adiabatic wall conditions were enforced on all solid walls.

3.2.1 Grid independency

Three grid scales, namely, coarse, medium, and refined grids, were utilized to analyze the grid independency in the simulation of the 2D inlet. Fig. 11 compares the wall pressure distributions under the three grid scales, where the black solid line represents the geometrical configuration of the inlet and the horizontal dashed-dotted line is the axis of symmetry. It can be seen that the wall pressure in the shock-dependent region remains unchanged and then gradually increases in the external compression region. Owing to the impingement of the cowl shock, the pressure curve rapidly rises at the inlet entrance. The three pressure curves are essentially the same, demonstrating that the main flow characteristics of isentropic compressions and shock/boundary layer interactions can be captured by the three grid scales. Table 1 lists the grid numbers and performance parameters of the inlet under different grid scales. The results show that the mass flow rates are exactly the same and all reach up to 1. However, the total pressure recovery coefficient under the coarse grid is 1.74% less than that under the refined grid. With an increase in the grid number, the total pressure recovery coefficient gradually converges, where the difference between the medium grid and refined grid is below 0.05%.

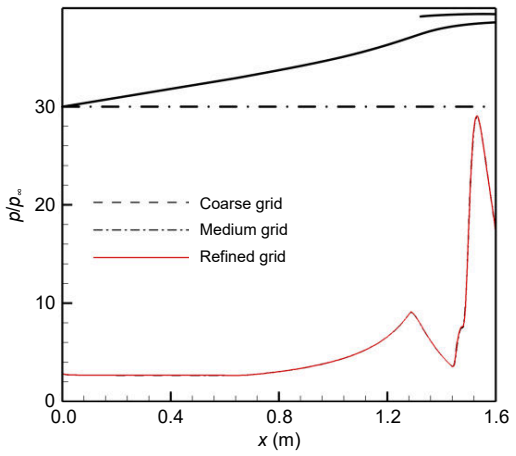

Fig. 11 Wall pressure distributions under three grid scales

Table 1 Grid numbers and inlet performance parameters under three grid scales

Grid scale	Grid number	φ	σ
Coarse	200×120	1.000	0.5684
Medium	300×180	1.000	0.5782
Refined	400×240	1.000	0.5785

In view of the excellent agreements on the wall pressure distributions and inlet performance parameters, the medium grid was chosen to solve the current 2D inlet flow fields. Moreover, the medium grid scale was adopted in every osculating plane of the 3D inlet flow fields. Finally, the grid numbers of the 2D and 3D inlets were 54000 and 3240000, respectively.

3.2.2 Code validation

The bump inlet was utilized as an experimental model to evaluate the accuracy of the proposed numerical method. The experiment was conducted in the free-jet wind tunnel with an inflow Mach number of 5 and attack angle of 0°. A series of pressure measurement holes were arranged along the flow direction in the symmetry plane of the inlet model. Pressure transducers with a range of 0–689 kPa were utilized to record the wall pressure signals. In addition, a schlieren system was applied to visualize the inlet flow field in the symmetry plane.

The proposed numerical method and grid setting were employed to simulate the experimental process. Fig. 12 compares the flow structures and wall pressure distributions obtained by the experiment and numerical simulation. The experimental and numerical results both indicate that an unblocked supersonic flow was formed at the inlet entrance, and the inlet was in the starting state. In addition, the forebody shock angles obtained by the experiment and numerical simulation were 15.4° and 15.6°, respectively, indicating good agreement. The pressure distributions of the two results were almost equal in the shock-dependent and external compression regions. Afterward, both pressure values rapidly rose at the inlet entrance and then fluctuated in the internal contraction region. The comparisons demonstrate that the proposed numerical method can capture the main flow characteristics of the inlet flow field.

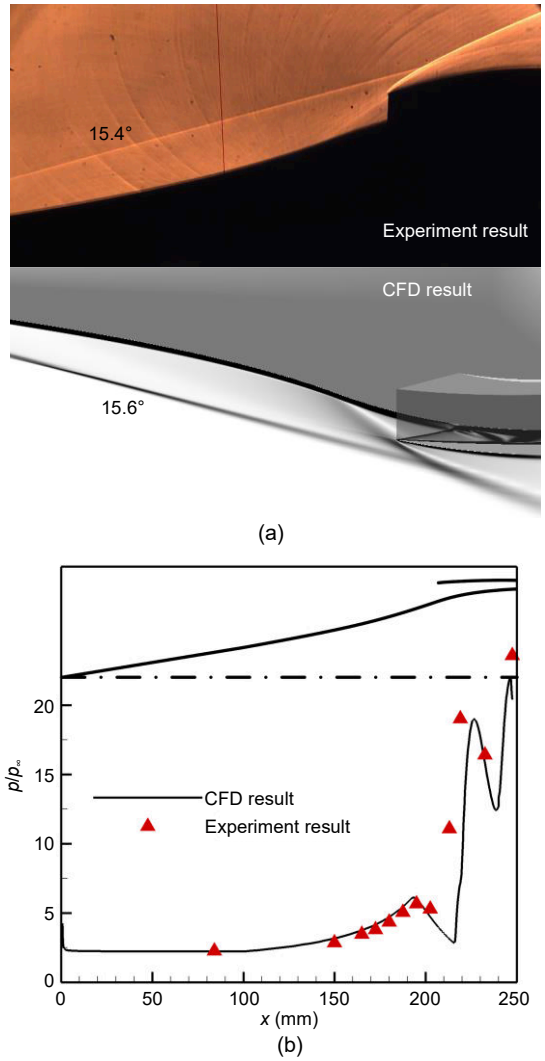

Fig. 12 Comparison of schlieren images (a) and wall pressure distributions (b) in the symmetry plane obtained by the experiment and the computational fluid dynamics (CFD) method

4 Results and discussion

4.1 Inlet performances under design conditions

The flow fields of the original and bump inlets were numerically simulated under the design conditions. The results show that the mass flow rate of the original inlet was 0.9960, essentially achieving full flow capture. Although the mass flow rate of the bump inlet decreased slightly, it still reached 0.9813. Moreover, the total pressure recovery coefficient of the original inlet was 0.5907, but that of the bump inlet reached up to 0.6138, which is 3.91% higher than that of the original inlet. Overall, the mass flow rate slightly decreased, but the total pressure recovery showed a significant improvement after designing the bump surface.

To reveal the reason for the changes in the performance parameters, the inlet flow structures were analyzed. Fig. 13 shows the Mach number contours in the osculating planes of θ=0°, 15°, 30°, and 45° for both inlets. The streamlines traced from the θ=45° osculating plane in the freestream flow field are also shown. The flow structures in all osculating planes of the original inlet were almost the same, and the inlet essentially maintained a 2D flow pattern. The forebody shock in each osculating plane impinged on the cowl leading edge, thereby achieving the shock-on-lip condition. Meanwhile, the streamlines traced from the θ=45° osculating plane practically intersected the leading edge of the sidewall, indicating that there was nearly no transverse spillage. Hence, the original inlet exhibited a high mass flow rate. Because the optimized feasible inlet configurations were adopted in

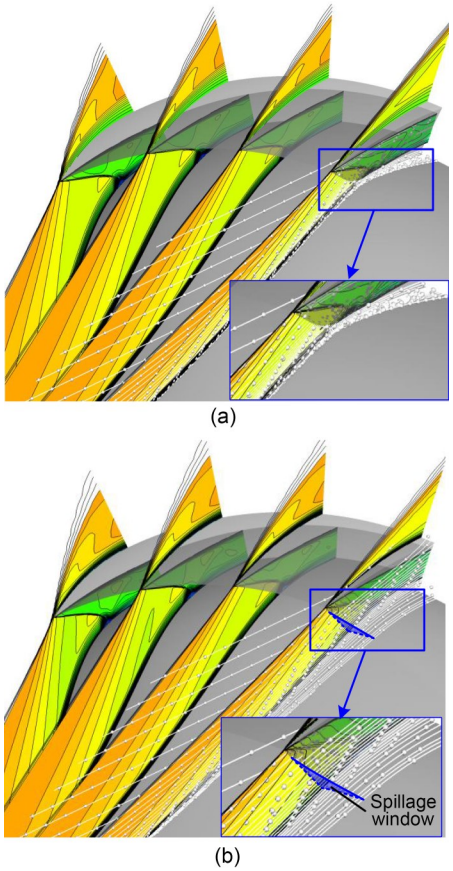

Fig. 13 Mach number contours in the osculating planes of θ=0°, 15°, 30°, and 45° and the streamlines traced from the θ=45° osculating plane in the freestream flow field: (a) original inlet; (b) bump inlet

the osculating planes, the shock-on-lip condition was also realized in the flow field of the bump inlet. However, most of the streamlines were excluded from the bump inlet. Additionally, the closer the streamline was to the wall, the larger the diversion scale was. Finally, a triangle-shaped spillage window (labeled in Fig. 13) was formed outside the sidewall. Since the near-wall low-energy airflow that should be captured by the inlet was excluded, the mass flow of the bump inlet slightly decreased but the total pressure recovery showed a significant improvement.

To evaluate the low-kinetic-energy flow diversion, the boundary layer heights of the original and bump inlets were compared. Considering the remarkable non-uniform flow characteristics in the current inlet flow field, the boundary layer was defined by the near-wall airflow, and the total pressure recovery coefficient was less than 0.3. Fig. 14a displays the distributions of the boundary layer in the cross-section immediately before the inlet entrance (in the plane of x=1.4 m), where the boundary flow is shown in blue and the main flow is shown in red. The boundary layer heights of both inlets are compared in Fig. 14b. The transverse flow of the original inlet is insignificant owing to the axisymmetric body. As a result,

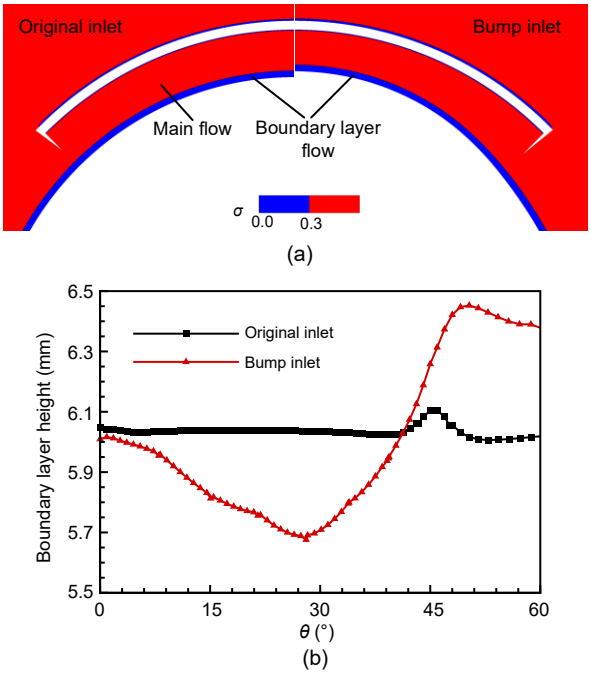

Fig. 14 Boundary layer distributions of the original and bump inlets in the plane of x=1.4 m: (a) boundary layer distributions; (b) comparison of boundary layer heights. References to color refer to the online version of this figure

the boundary layer height remained almost constant (6.04 mm), except for a slight fluctuation due to the sidewall around θ=45°. In contrast, the boundary layer height of the bump inlet significantly changed along the transverse direction. Specifically, its height gradually decreased and reached the minimum value of 5.68 mm near θ=30°, which is also the position of the maximal TPG. The results also show that the largest transverse spillage speed (approximately 118.3 m/s) also appeared near θ=30°. As the TPG decreased, the velocity of the transverse flow gradually decreased beyond θ=30°. Correspondingly, the boundary layer height continuously grew and reached the highest value of 6.45 mm at θ=50.3°. In summary, due to the diversion effect of the bump, the boundary layer was thinner in the inlet capture region but thicker outside the inlet. In other words, the boundary layer airflow that should be swallowed by the inlet was successfully excluded from the inlet.

4.2 Inlet starting performance

4.2.1 Starting process

The proposed numerical method was utilized to calculate the inlet accelerating self-starting process. Fig. 15 displays the Mach number contours in the symmetry plane of both inlets at typical Mach numbers. When the Mach number was 3.0, large-scale separation bubbles were formed, and separation shocks were induced in both inlet flow fields. The forming mechanism of the large-scale separation bubble is described as follows. According to the Kantrowitz and isentropic limits, the airflow choked at the throat when the incoming Mach number was low. Consequently, a high-pressure signal was formed at the throat and then moved upstream. When the high-pressure signal arrived at the position of the cowl lip shock/boundary layer interactions, the separation bubble scale greatly increased due to an increasing adverse pressure gradient. Finally, a large-scale separation bubble was established on the compression surface. As can be seen, the series of incoming airflow were deflected upstream of the inlet entrances and spilled above the cowl lip, leading to a decline in the captured airflow. Clearly, both inlets were in an unstarting state. As the inflow Mach number increased to 3.5, although the separation bubbles shrank and moved downstream, the flow structures exhibited no substantial change. However, the large-scale separation zone

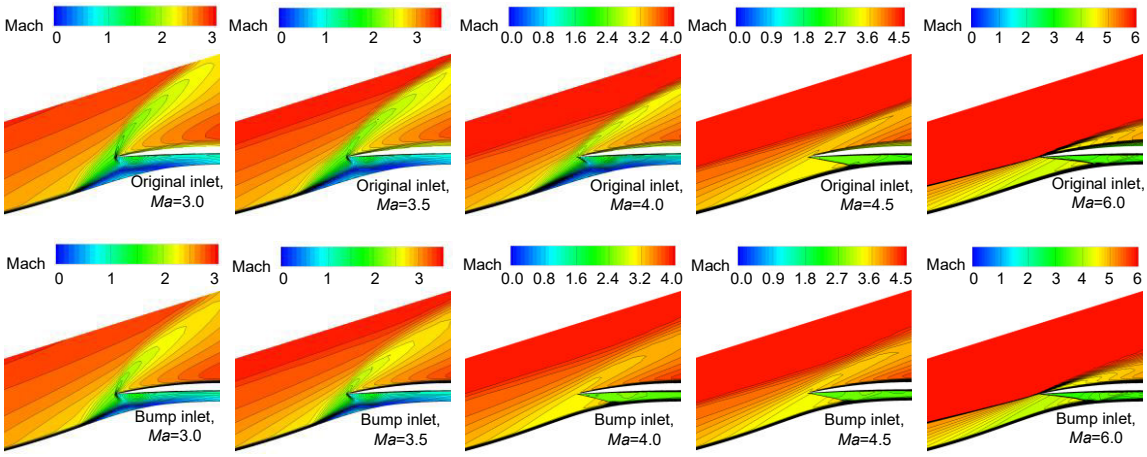

Fig. 15 Mach number contours in the symmetry plane at typical incoming Mach numbers

of the bump inlet completely vanished at *Ma*=4.0. Consequently, the mass flow was not influenced by the inlet flow in the internal portion, and an unblocked supersonic flow was established in the entire duct, implying that the inlet entered the starting state. In contrast, there was a large-scale separation bubble in the original inlet until the Mach number increased from 4.0 to 4.5.

Large-scale separation bubbles play a key role in the inlet starting process. With an increase in the inflow Mach number, the separation bubble shrank and moved downstream with increasing incoming dynamic pressure. When the Mach number increased to a certain value, the separation bubble could not self-sustain and was eventually swallowed.

Fig. 16 shows the distributions of mass flow rate and total pressure recovery coefficient during the starting process. The two parameters of both inlets are relatively low at *Ma*=3.0. As the incoming flow accelerated, continuous rises could be seen in the mass flow rates, but the total pressure recovery coefficients noticeably decreased because of the growing intensity of the shock waves. It is noted that the mass flow rate and total pressure recovery coefficient of the bump inlet were both higher than those of the original inlet in the unstarting state, as discussed later in Section 4.2.3. As the Mach number increased from 3.94 to 3.95, the mass flow rate of the bump inlet rapidly increased, and the total pressure recovery coefficient increased to 0.73. Also, the parameters of the original inlet experienced similar jumps with the increase in Mach number from 4.34 to 4.35. The reason for the sudden improvements of inlet performance parameters is that the separation bubble disappeared and the inlet entered the starting state. Therefore, the starting Mach numbers (Ma_s) of the original and bump inlets were 4.35 and 3.95, respectively. This demonstrates that the starting Mach number was reduced by 0.4 by designing the bump surface, which effectively broadens the inlet operating range.

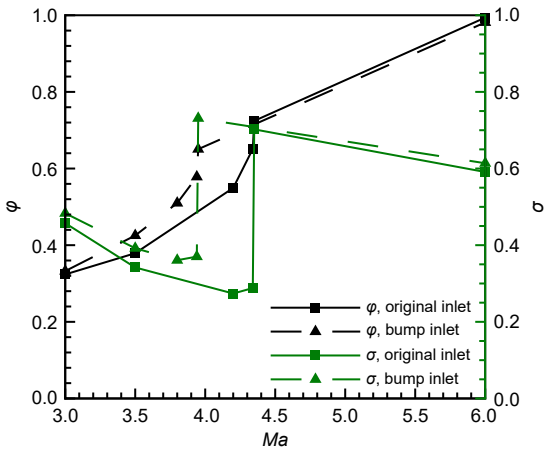

Fig. 16 Distributions of mass flow rate and total pressure recovery coefficient during starting process

4.2.2 Experimental study on near-wall shape of separation bubble

To reveal the flow mechanism of the improvement in the bump inlet starting performance, the near-wall flow of the separation bubble in the unstarting state was experimentally investigated. Because the ability to change the inflow Mach number is limited, it is difficult to obtain the unstarting flow field under the current experimental conditions. According to previous

studies, the unstarting flow field caused by a low Mach number can be well-simulated by giving a high attack angle (Guo et al., 2017). Therefore, in this study, the inlet was pre-installed at a high angle of attack to acquire the unstarting flow field.

Oil flow experiments were performed in the wind tunnel to visualize the near-wall flow. Methyl silicone oil was utilized, and white nanoparticles were added to improve the contrast. Two oil flow experiments were conducted on the original inlet and bump inlet at an inflow Mach number of 5 and attack angle of 6°.

The mixed oil was uniformly smeared on the inlet surfaces before testing. When high-speed incoming air flowed through the wall surface, the oil was suddenly pushed downstream. However, a large-scale separation zone was formed at the inlet entrance because of the emergence of an inlet unstart. The flow direction of the near-wall air in the separation zone was opposite to that of the main flow. As a result, oil accumulated at the initial position of the separated flow. Fig. 17 shows the oil flow distributions on the walls of the original and bump inlets at the unstarting state from a top-down view. The white lines in the figure represent the separation lines of the large-scale separation bubbles. As can be seen, the separation line of the original inlet maintains good 2D characteristics in the central region. Then, it gradually moves downstream at the two sides because of the spillage, forming an arc-shaped separation line along the transverse direction. On the contrary, the separation line of the bump inlet is mainly characterized by downstream movement in the central area and rapid upstream movements at the two sides. In general, compared with the original inlet, the separation zone scale of the bump inlet was significantly reduced in the inlet capture range.

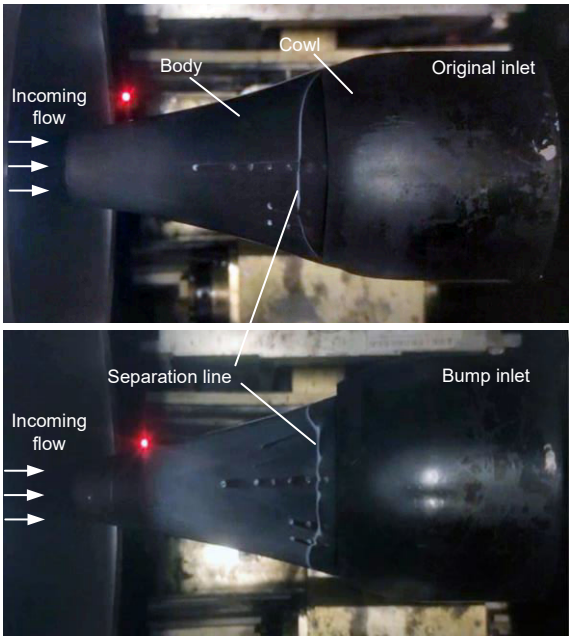

Fig. 17 Oil flow distributions on the walls of both inlets at unstarting state from a top-down view

4.2.3 Three-dimensional rebuilding effect of bump on the separation bubble

Fig. 18 displays the Mach number contours in different osculating planes of both inlets at a relatively low Mach number of 3.5. The separation zone scale of the original inlet was relatively large near the symmetry plane, leading to a considerable spillage above the cowl lip. However, the separation bubble gradually moved downstream, and its height decreased along the transverse direction. Consequently, the separation shock gradually moved closer to the cowl, and the scale of the cowl lip spillage significantly decreased from the middle to the side. Regarding the bump inlet,

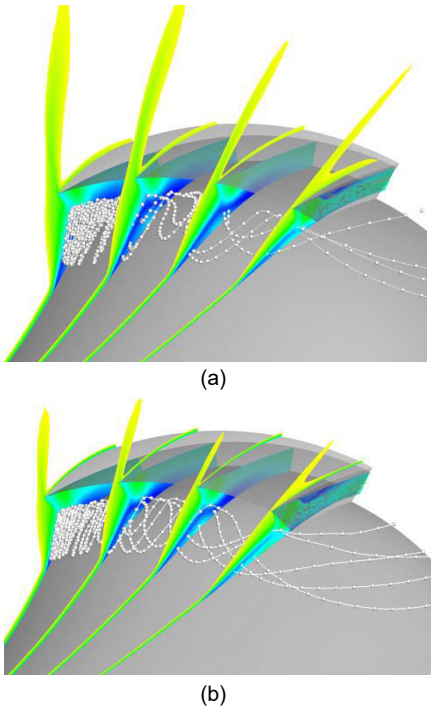

Fig. 18 Mach number contours in the osculating planes of θ=0°, 15°, 30°, and 45° and streamline distributions in the separation bubble at Ma=3.5: (a) original inlet; (b) bump inlet

cowl lip spillage also formed near the symmetry plane, but its scale was significantly less than that of the original inlet. In addition, although the separation bubble length gradually increased along the transverse direction, the cowl lip spillage at the side was substantially reduced because of the drop in separation bubble height. Overall, the separation shock intensity of the bump inlet was weaker, and the cowl lip spillage scale was smaller than that of the original inlet. This is why the mass flow rate and total pressure recovery coefficient of the bump inlet were both higher than those of the original inlet in the unstarting state.

As shown in Fig. 18, the quasi-helical streamlines were distributed in the large-scale separation bubbles of both inlets and were eventually excluded. The airflow in the separation bubble was characterized by the separation vortices near the symmetry plane but was dominated by the transverse spillage near the sidewall. This is because the static pressure in the separation bubble was notably higher than that outside. Driven by the pressure difference, the transverse flow significantly accelerated at the side. Under the combined effect of the separation vortex and transverse spillage, quasi-helical streamlines were finally formed in the separation bubble.

Fig. 19 shows the TPG distributions in the separation bubbles of both inlets (in the plane of x=1.35 m). Under the pressure difference between the inside and outside of the separation zone, the TPG of the original inlet rapidly dropped outside the sidewall. In contrast, there was a considerable TPG decline in the capture region of the bump inlet, owing to not only the pressure drop caused by the separation bubble but also the pressure drop from the bump. The pressure difference in the inlet capture region of the original inlet was only $1.02p_\infty$, but that of the bump inlet reached $1.65p_\infty$. In addition, the absolute maximum of the TPG in the bump inlet occurred near the sidewall, which can significantly accelerate the transverse spillage. Fig. 20 shows the transverse velocity (V_t) distributions in the plane of x=1.35 m. The range and velocity of the transverse spillage in the bump inlet flow field were notably larger than those of the original inlet, where the maximum transverse velocity of the bump inlet reached up to 461.5 m/s. This means that more airflow in the separation zone of the bump inlet was excluded. Therefore, the separation bubble shrank notably, thereby promoting the inlet start.

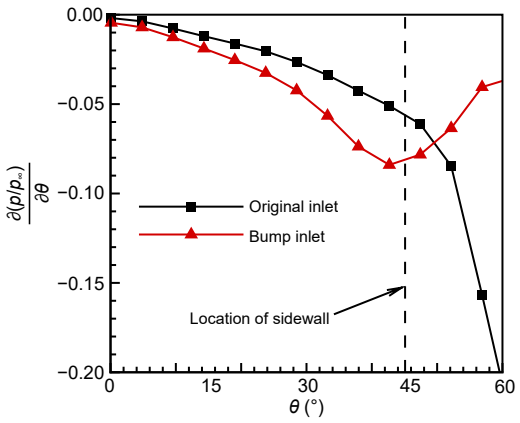

Fig. 19 TPG distributions in the plane of x=1.35 m at Ma=3.5

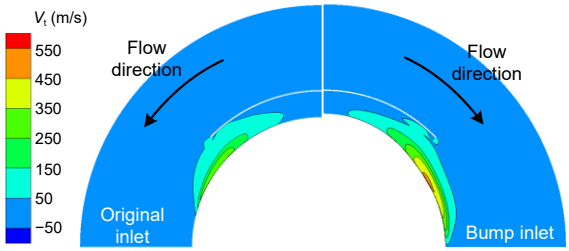

Fig. 20 Transverse velocity (V_t) contours in the plane of x=1.35 m at Ma=3.5

4.3 Mass flow correction for the bump inlet

According to the working mechanism of the bump, the near-wall boundary layer was diverted so that the captured airflow quality was improved. However, the bump also led to a slight decline in the mass flow rate under the design conditions. To increase the inlet mass flow to the designed level, mass flow correction was conducted on the bump inlet. In view of the constraints in the inlet integrated design, the following requirements should be met during the mass flow correction: the shock-on-lip condition should be maintained under the design conditions, the location and shape of the inlet throat should remain unchanged, and the bump configuration should remain intact. To increase the inlet mass flow, a feasible correction method was used to enlarge the inlet capture area. Considering the above requirements, a method that extends the inlet center angle was adopted. Fig. 21 schematically illustrates the bump inlet capture area before and after the mass flow correction. As shown, the center angle increased from 90.0° to 91.4° via correction. It should be noted that slight side compressions are

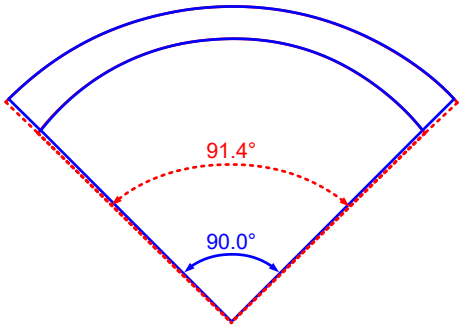

Fig. 21 Diagram of the capture area of the bump inlet before (solid) and after (dashed) mass flow correction

inevitably introduced by the sidewalls of the corrected bump inlet. Through a reasonable design, a series of weak isentropic compression waves were generated by the sidewalls without a shock system.

Table 2 lists the geometric and aerodynamic parameters of the inlets. The mass flow rate of the corrected bump inlet reached as high as 0.9993, indicating that the proposed correction method is effective. Besides, because the bump surface was unchanged, the low-energy boundary layer was also excluded, resulting in an almost constant high total pressure recovery coefficient. Moreover, the starting performance slightly declined after the correction because of the increase of inlet capture area. However, the starting Mach number of the corrected bump inlet was still 0.26 lower than that of the original inlet.

Table 2 Geometric and aerodynamic parameters of the inlets

Inlet	Center angle	φ	σ	Ma_s
Original inlet	90.0°	0.9960	0.5907	4.35
Bump inlet	90.0°	0.9813	0.6138	3.95
Corrected bump inlet	91.4°	0.9993	0.6122	4.09

5 Conclusions

This study developed a novel method for designing a hypersonic bump inlet based on a given TPG. The proposed design method was applied to a hypersonic chin inlet, and the main performance parameters of the acquired bump inlet were investigated. The following conclusions were drawn:

1. The designed bump configuration was highly integrated with the inlet compression wall without additional flow loss under hypersonic conditions. In addition, this method provides a potential means to directly control the aerodynamic parameters of the bump rather than the geometric parameters.

2. The boundary layer flow was excluded from the inlet capture range owing to the TPG on the bump surface. As a result, the mass flow of the bump inlet slightly decreased, but the total pressure recovery showed a significant improvement.

3. The bump had a 3D rebuilding effect on the large-scale separation bubble in the unstarting state. In addition, the TPG on the bump surface greatly accelerated the transverse spillage in the separation bubble, which substantially improved the inlet starting ability.

4. Full flow capture was successfully achieved in the bump inlet by performing the proposed mass flow correction. Compared with the original inlet, the corrected bump inlet still had obvious advantages in terms of total pressure recovery performance and starting ability.

Acknowledgments

This work is supported by the National Natural Science Foundation of China (No. 12102470) and the Hunan Provincial Innovation Foundation for Postgraduate (No. CX20200082), China.

Author contributions

Shang-cheng XU, Yi WANG, and Zhen-guo WANG designed the research. Shang-cheng XU and Bing XIONG processed the corresponding data. Shang-cheng XU wrote the first draft of the manuscript. Bing XIONG helped to organize the manuscript. Yi WANG and Xiao-qiang FAN revised and edited the final version.

Conflict of interest

Shang-cheng XU, Yi WANG, Zhen-guo WANG, Xiao-qiang FAN, and Bing XIONG declare that they have no conflict of interest.

References

Bhanderi H, Babinsky H, 2005. Improved boundary layer quantities in the shock wave boundary layer interaction region on bumps. Proceedings of the 35th AIAA Fluid Dynamics Conference and Exhibit. https://doi.org/10.2514/6.2005-4896

Cheng SX, Zhan H, Shu ZX, et al., 2019. Effective optimization on bump inlet using meta-model multi-objective particle swarm assisted by expected hyper-volume improvement. *Aerospace Science and Technology*, 87:431-447. https://doi.org/10.1016/j.ast.2019.02.039

Colliss SP, Babinsky H, Nübler K, et al., 2014. Joint experimental and numerical approach to three-dimensional

shock control bump research. *AIAA Journal*, 52(2):436-446.
https://doi.org/10.2514/1.J052582

Curran ET, 2001. Scramjet engines: the first forty years. *Journal of Propulsion and Power*, 17(6):1138-1148.
https://doi.org/10.2514/2.5875

Curran ET, Murthy SNB, 2001. Scramjet Propulsion. American Institute of Aeronautics and Astronautics, Reston, USA, p.462-466.
https://doi.org/10.2514/4.866609

Ding F, Liu J, Shen CB, et al., 2018. An overview of waverider design concept in airframe/inlet integration methodology for air-breathing hypersonic vehicles. *Acta Astronautica*, 152:639-656.
https://doi.org/10.1016/j.actaastro.2018.09.002

Guo ST, Li ZF, Gao WZ, et al., 2017. Analogy between effects of attack angle and Mach number on inlet starting. *Journal of Propulsion Technology*, 38(5):983-991 (in Chinese).
https://doi.org/10.13675/j.cnki.tjjs.2017.05.004

Huang GP, Zuo FY, Qiao WY, 2018. Design method of internal waverider inlet under non-uniform upstream for inlet/forebody integration. *Aerospace Science and Technology*, 74:160-172.
https://doi.org/10.1016/j.ast.2018.01.012

Huang W, Chang JT, Yan L, 2020. Mixing and combustion in supersonic/hypersonic flows. *Journal of Zhejiang University-SCIENCE A (Applied Physics & Engineering)*, 21(8):609-613.
https://doi.org/10.1631/jzus.A20MCSF1

Im SK, Do H, 2018. Unstart phenomena induced by flow choking in scramjet inlet-isolators. *Progress in Aerospace Sciences*, 97:1-21.
https://doi.org/10.1016/j.paerosci.2017.12.001

Johnson CB, Lawing PL, 1977. Mach 6 flowfield survey at the engine inlet of a research airplane. *Journal of Aircraft*, 14(4):412-414.
https://doi.org/10.2514/3.44604

Kim J, Sung HJ, 2006. Wall pressure fluctuations in a turbulent boundary layer over a bump. *AIAA Journal*, 44(7):1393-1401.
https://doi.org/10.2514/1.6519

Kim SD, 2009. Aerodynamic design of a supersonic inlet with a parametric bump. *Journal of Aircraft*, 46(1):198-202.
https://doi.org/10.2514/1.37416

Kim SD, Song DJ, 2007. A numerical analysis on three-dimensional flow field in a supersonic bump-type inlet. *Journal of Mechanical Science and Technology*, 21(2):327-335.
https://doi.org/10.1007/BF02916293

Kim SD, Song DJ, 2008. Numerical study on performance of supersonic inlets with various three-dimensional bumps. *Journal of Mechanical Science and Technology*, 22(8):1640-1647.
https://doi.org/10.1007/s12206-008-0503-9

Lau KY, 2008. Hypersonic boundary-layer transition: application to high-speed vehicle design. *Journal of Spacecraft and Rockets*, 45(2):176-183.
https://doi.org/10.2514/1.31134

Lawing PL, Johnson CB, 1978. Inlet boundary-layer shapes on four aircraft forebodies at Mach 6. *Journal of Aircraft*, 15(1):62-63.
https://doi.org/10.2514/3.58313

Li YQ, Zheng XG, Shi CG, et al., 2020. Integration of inward-turning inlet with airframe based on dual-waverider concept. *Aerospace Science and Technology*, 107:106266.
https://doi.org/10.1016/j.ast.2020.106266

Liu JB, Fan XQ, Tao Y, et al., 2019. Experimental and numerical study on the local unstart mechanism of hypersonic inlet. *Acta Astronautica*, 160:216-221.
https://doi.org/10.1016/j.actaastro.2019.04.041

Lo KH, Kontis K, 2017. Flow characteristics of various three-dimensional rounded contour bumps in a Mach 1.3 freestream. *Experimental Thermal and Fluid Science*, 80:228-243.
https://doi.org/10.1016/j.expthermflusci.2016.08.027

Saheby EB, Huang GP, Qiao WY, et al., 2016. Highly integrated inlet design based on the ridge concept. *Journal of Propulsion and Power*, 32(6):1505-1515.
https://doi.org/10.2514/1.B36009

Saheby EB, Huang GP, Hays A, 2017. Design of hypersonic forebody by the combination of bump and waverider surfaces. Proceedings of the 21st AIAA International Space Planes and Hypersonics Technologies Conference.
https://doi.org/10.2514/6.2017-2177

Schwartz MJ, Gaitonde D, Slater J, 2021. Effects of bleed on supersonic turbulent boundary layers. Proceedings of the AIAA Aviation Forum.
https://doi.org/10.2514/6.2021-2885

Simon PC, Brown DW, Huff RG, 1957. Performance of External-Compression Bump Inlet at Mach Numbers of 1.5 and 2.0. Report No. NACA-RM-E56L19, National Advisory Committee for Aeronautics, USA.

Su WY, Chen Y, Zhang FR, et al., 2018. Control of pseudo-shock oscillation in scramjet inlet-isolator using periodical excitation. *Acta Astronautica*, 143:147-154.
https://doi.org/10.1016/j.actaastro.2017.10.040

Svensson M, 2008. A CFD Investigation of a Generic Bump and Its Application to a Diverterless Supersonic Inlet. MS Thesis, Linköping University, Linköping, Sweden.

Sziroczak D, Smith H, 2016. A review of design issues specific to hypersonic flight vehicles. *Progress in Aerospace Sciences*, 84:1-28.
https://doi.org/10.1016/j.paerosci.2016.04.001

Tillotson BJ, Loth E, Dutton JC, et al., 2009. Experimental study of a Mach 3 bump-compression flowfield. *Journal of Propulsion and Power*, 25(3):545-554.
https://doi.org/10.2514/1.35306

Trefny CJ, 1999. An air-breathing launch vehicle concept for single-stage-to-orbit. Proceedings of the 35th Joint Propulsion Conference and Exhibit.
https://doi.org/10.2514/6.1999-2730

Xiong B, Fan XQ, Wang Y, 2019. Parameterization and optimization design of a hypersonic inward turning inlet. *Acta Astronautica*, 164:130-141.

https://doi.org/10.1016/j.actaastro.2019.07.004

Xu SC, 2018. Design and Analysis of Hypersonic Inlet with Integrated Bump/Forebody. MS Thesis, National University of Defense Technology, Changsha, China (in Chinese).

Xu SC, Wang Y, Wang ZG, et al., 2017. The design and analysis of bump in high speed supersonic flow. Proceedings of the 21st AIAA International Space Planes and Hypersonics Technologies Conference. https://doi.org/10.2514/6.2017-2269

Xu SC, Wang Y, Wang ZG, et al., 2019. Design and analysis of a hypersonic inlet with an integrated bump/forebody. *Chinese Journal of Aeronautics*, 32(10):2267-2274. https://doi.org/10.1016/j.cja.2019.04.010

Yang YK, 2007. The research of bump inlet design and test. *Acta Aerodynamica Sinica*, 25(3):336-338 (in Chinese). https://doi.org/10.3969/j.issn.0258-1825.2007.03.010

Yu ZH, Huang GP, Xia C, 2018. Inverse design and Mach 6 experimental investigation of a pressure controllable bump. *Aerospace Science and Technology*, 81:204-212. https://doi.org/10.1016/j.ast.2018.08.006

Yu ZH, Huang GP, Xia C, et al., 2019. A pressure-controllable bump based on the pressure-ridge concept. *Aerospace Science and Technology*, 87:133-140. https://doi.org/10.1016/j.ast.2019.02.015

Yu ZH, Huang GP, Xia C, 2020. 3D inverse method of characteristics for hypersonic bump-inlet integration. *Acta Astronautica*, 166:11-22. https://doi.org/10.1016/j.actaastro.2019.09.015

Yuan HC, Liu FZ, Wang X, et al., 2021. Design and analysis of a supersonic axisymmetric inlet based on controllable bleed slots. *Aerospace Science and Technology*, 118:107008. https://doi.org/10.1016/j.ast.2021.107008

Yue LJ, Jia YN, Xu X, et al., 2018. Effect of cowl shock on restart characteristics of simple ramp type hypersonic inlets with thin boundary layers. *Aerospace Science and Technology*, 74:72-80. https://doi.org/10.1016/j.ast.2017.12.018

Zhang BH, Zhao YX, Liu J, 2020. Effects of bleed hole size on supersonic boundary layer bleed mass flow rate. *Journal of Zhejiang University-SCIENCE A (Applied Physics & Engineering)*, 21(8):652-662. https://doi.org/10.1631/jzus.A1900507

Zhang Y, Tan HJ, Tian FC, et al., 2014. Control of incident shock/boundary-layer interaction by a two-dimensional bump. *AIAA Journal*, 52(4):767-776. https://doi.org/10.2514/1.J052786